







RESEARCH ARTICLE | JULY 15 2024

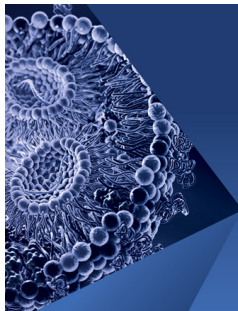
## Rotationally induced ingress in rotor–stator systems

D. Graikos  ; H. Tang  ; M. Carnevale  ; N. Y. Bailey  ; J. A. Scobie  



*Physics of Fluids* 36, 075141 (2024)

<https://doi.org/10.1063/5.0207140>



## Physics of Fluids

Special Topic:

Flow and Lipid Nanoparticles

Guest Editors: Richard Braatz and Mona Kanso

[Submit Today!](#)

# Rotationally induced ingress in rotor–stator systems

Cite as: Phys. Fluids **36**, 075141 (2024); doi: [10.1063/5.0207140](https://doi.org/10.1063/5.0207140)

Submitted: 6 March 2024 · Accepted: 10 June 2024 ·

Published Online: 15 July 2024



View Online



Export Citation



CrossMark

D. Graikos,<sup>1</sup> H. Tang,<sup>1</sup> M. Carnevale,<sup>1</sup> N. Y. Bailey,<sup>2</sup> and J. A. Scobie<sup>1,a)</sup>

## AFFILIATIONS

<sup>1</sup>Department of Mechanical Engineering, University of Bath, Bath BA2 7AY, United Kingdom

<sup>2</sup>Department of Engineering, King's College London, London WC2R 2LS, United Kingdom

<sup>a)</sup> Author to whom correspondence should be addressed: [j.a.scobie@bath.ac.uk](mailto:j.a.scobie@bath.ac.uk)

## ABSTRACT

The presence of a rotating disk adjacent to a stationary disk forms a rotor–stator cavity known as a wheel-space. It is necessary for gas turbine wheel-spaces to be purged with sealing flow bled from the compressor to counteract the harmful effects of ingress. This paper presents a combined experimental, theoretical, and computational study of rotationally induced ingress in rotor–stator systems. Measurements were made in a wheel-space with an axial clearance rim seal under axisymmetric conditions in the absence of a mainstream annulus through-flow. Ingress was quantified using a gas concentration technique and the flow structure in the cavity was explored with static and total pressure measurements to determine the swirl ratio. A low-order theoretical model was developed based on the boundary layer momentum-integral equations. The theory gave excellent results when predicting the effects of ingress and purge flows on the radial pressure and swirl gradients. Unsteady Reynolds-Averaged Navier–Stokes computations were conducted to provide greater fluid dynamic insight into the wheel-space flow structure and ingress through the rim seal. The computational results demonstrated some of the closest agreement with experimental measurements of ingress available in the literature, showing that rotationally induced ingress is dominated by unsteady large-scale structures in the rim seal gap instead of the previously ascribed disk-pumping effect. The study serves as an important validation case for investigations of ingress in rotor–stator systems in more complex environments.

© 2024 Author(s). All article content, except where otherwise noted, is licensed under a Creative Commons Attribution (CC BY) license (<https://creativecommons.org/licenses/by/4.0/>). <https://doi.org/10.1063/5.0207140>

## NOMENCLATURE

|              |  |
|--------------|--|
| $a, b$       | inner, outer radius of disks                                 |
| $C_p$        | non-dimensional pressure                                     |
| $C_w$        | dimensionless purge flow parameter ( $= \dot{m}_0 / \mu b$ ) |
| $c$          | concentration of CO <sub>2</sub>                             |
| $G_c$        | gap ratio of cavity  |
| $\dot{m}$    | mass flow rate   |
| $p$          | pressure   |
| $Re_\phi$    | Reynolds number  |
| $r, \phi, z$ | coordinate system (radial, tangential, axial)                |
| $S$          | axial distance between rotor and stator                      |
| $s_c$        | clearance of rim seal  |
| $V$          | velocity of solid surface                                    |
| $v$          | air velocity   |
| $v_r^*$      | maximum radial velocity in boundary layers                   |
| $x, \eta$    | dimensionless radial and axial coordinates                   |
| $z$          | axial coordinate   |

|                     |  |
|---------------------|--|
| $\alpha$            | ratio of velocities                                |
| $\beta$             | swirl ratio (dimensionless tangential velocity)    |
| $\gamma$            | dimensionless boundary layer thickness coefficient |
| $\delta$            | dimensionless boundary layer thickness             |
| $\varepsilon$       | sealing effectiveness                              |
| $\lambda$           | dimensionless mass flow rate (viscous)             |
| $\mu$               | dynamic viscosity                                  |
| $\rho$              | density  |
| $\tau_r, \tau_\phi$ | radial, tangential shear stress                    |
| $\Phi$              | dimensionless mass flow rate (inertial)            |
| $\Omega$            | angular velocity of rotor                          |

## Subscripts

|        |                    |
|--------|--------------------|
| $a, b$ | inner, outer radii |
| $ax$   | axial              |
| $c$    | concentration      |
| $I$    | ingress            |

$R, S$  rotor, stator  
 $ref$  appropriated reference values  
 $r, \phi, z$  coordinate system (radial, tangential, axial)  
 $0$  purge flow

I. INTRODUCTION

Ultrahigh efficiency is important in the quest toward reduced CO<sub>2</sub> emissions for aviation and land-based power generation, while the pressing global warming challenges lead gas turbine engine manufacturers toward sustainable solutions to reduce fuel consumption. A greater fundamental understanding of fluid dynamics and heat transfer is crucial to achieve these targets as these determine the integrity and thermal efficiency of gas turbine components.

Rotor–stator systems are present in a wide variety of engineering applications; examples include turbomachinery, computing hardware, braking systems, particle separators, medical devices, and food processing. A rotor–stator system in a gas turbine consists of stationary and rotating disks forming a cavity delimited by a hub and shroud in the inner and outer regions, respectively, as shown in Fig. 1. The typical flow structure in a rotor–stator cavity, also called a wheel-space, is depicted in Fig. 2. Ingress, which refers to the hot gas ingested into the cavity, can penetrate via a rim seal at the shroud. The temperature of the ingress can be significantly higher than the melting point of the metal components, affecting the life of the turbine. To prevent hot gas ingestion, cool pressurized air called purge flow is provided through the secondary air system at the lower portion of the cavity. Under-purging can catastrophically affect the integrity of the materials, while over-purging the cavity significantly reduces the thermal and aerodynamic efficiency of the engine. Ingress is modulated by rotating coherent structures arising from interaction with the purge flow in the rim-seal region.

The physical mechanisms that govern ingress in gas turbine wheel-spaces are complex and still not fully understood. Classically, there are two types of turbine rim seal ingestion: (1) disk “pumping”

or rotationally induced (RI) ingress and (2) non-axisymmetric pressure-driven or externally induced (EI) ingress. Both mechanisms treat ingress as a result of balancing the radial pressure gradient and the centrifugal forces.

Recently, experimental and computational studies have demonstrated the presence of large-scale unsteady structures in rim seals. It has been shown that capturing this unsteadiness is essential for accurate prediction of the ingress. The unsteady structures have been attributed to Kelvin–Helmholtz instabilities, Taylor–Couette instabilities, Rayleigh–Taylor instabilities, and inertial waves by different researchers.

In this paper, rotationally induced (RI) ingress has been studied to enhance the understanding of the flow phenomena that occur in a simplified environment. It is demonstrated that this is an important validation case to consider before attempting to analyze more complex scenarios. The University of Bath 1.5-stage axial turbine rig was modified to isolate any effects of vanes, blades, and annulus flow. A canonical rotor–stator system was studied, with ingress quantified using pressure and gas concentration measurements. Computational fluid dynamics (CFD) was conducted to provide greater insight into the fundamental fluid dynamics associated with the problem. A low-order theoretical approach was also developed as a modeling tool for expedient engine design calculations.

A review of the research on the ingress and flow structures in rotor–stator cavities is provided in Sec. II. Section III presents the experimental, computational, and theoretical methodologies used in this study to enhance the understanding of ingress and cavity flows. The discussion of the measurements, theoretical modeling, and computational simulations is given in Sec. IV. Section V summarizes the conclusions.

II. LITERATURE REVIEW

Previous research has been conducted to investigate and understand the flow physics within rotor–stator systems. Typically,

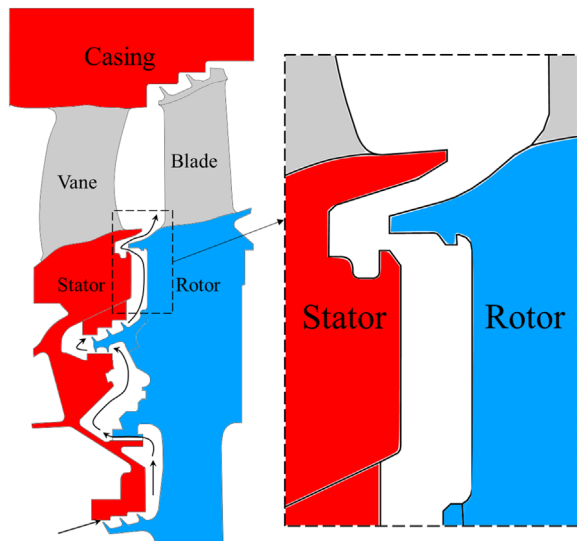


FIG. 1. A typical gas turbine stage with a magnified view of the rim-seal region.

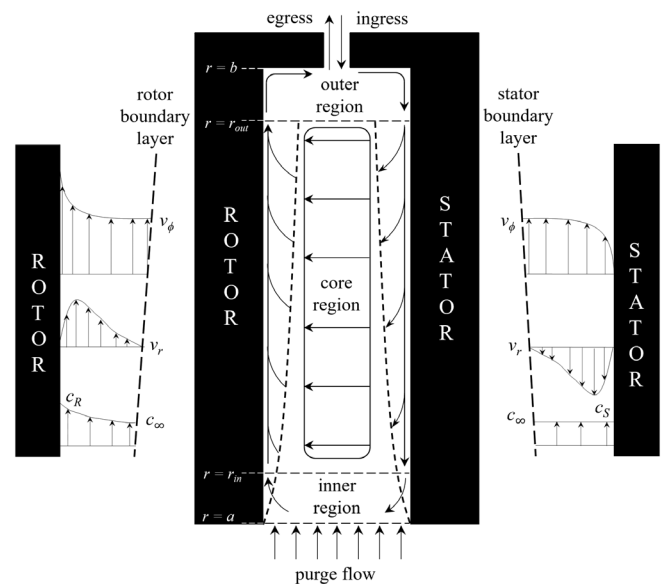


FIG. 2. Rotor–stator system with boundary layers, rotating core, velocity, and concentration profiles.

16 September 2024 07:27:47

experiments are performed to identify the effects of rim seal geometries and operating conditions on ingress and wheel-space flows. Low-order empirical models have been developed to predict these flows, and computational codes have been used to investigate the detailed flow behavior. This review focuses on RI ingress, which is the regime considered in this research. Detailed reviews of ingress research more generally can be found in Scobie *et al.*<sup>1</sup> and Chew *et al.*<sup>2</sup>

Bayley and Owen<sup>3</sup> presented the first RI experimental study on ingress using a simple axial clearance rotor–stator system open to the atmosphere. Pressure measurements were used to determine the minimum amount of purge flow to prevent ingress, with sub-atmospheric readings indicating ingestion had taken place. It was found the minimum flow rate required increased with increasing seal clearances and rotational speeds.

Phadke and Owen<sup>4</sup> extended the previous study by incorporating flow visualization and gas concentration measurements; the characteristics of seven rotor–stator geometries were considered. For all seven seals, the required purge flow rate to prevent ingress increased with rotational speed and with seal clearance. Chew *et al.*<sup>5</sup> used pressure measurements to determine the minimum purge flow rate required to prevent RI ingress for three different seals. They showed the seals with an extended lip on the rotor provided the most protection from ingress.

RI ingress has been quantified experimentally using concentration measurements as described in Graber *et al.*<sup>6</sup> The variation of sealing effectiveness,  $\varepsilon$ , with the purge flow rate for different seals was presented. This is equivalent to an adiabatic effectiveness through the application of the mass transfer analogy.

At Bath, Sangan *et al.*<sup>7</sup> also experimentally measured RI ingress into the cavity of a turbine stage using gas concentration measurements. Using a non-dimensional sealing parameter  $\Phi_0$ , effectiveness data collected for different rotational speeds were shown to collapse onto a single curve.

Mear-Stone<sup>8</sup> compared the measurements made in the Bath rig with predicted swirl and pressure distributions using a mathematical model based on the momentum-integral equations. Generally, good agreement was achieved with the largest difference near the rim seal. The mathematical model was further developed by Bailey *et al.*<sup>9</sup> to show that the swirl distributions can be modified by ingress. This effect of ingress could have been responsible for the difference in swirl near the seal presented by Mear-Stone.

Beard *et al.*<sup>10</sup> conducted unsteady pressure measurements of the flow in the rim seal gap under RI conditions on a rotor–stator system with a chute seal. A distinct peak frequency was found at around 23 times the disk speed from the Fast Fourier Transform analysis of the pressure data. Cross correlation of six circumferentially separated unsteady probes in the wheel-space showed 26–29 structures rotating at approximately 0.8 times the speed of the disk. The number of structures reduced slightly with increasing purge flow rate. The paper showed experimental evidence of the existence of large-scale structures that could have impacts on ingress flows.

Gao *et al.*<sup>11</sup> carried out a numerical investigation of the flow structures observed in the experimental rig employed by Beard *et al.*<sup>10</sup> They performed simulations using unsteady Reynolds-Averaged Navier–Stokes (URANS) and large-eddy simulation (LES) solvers. Both URANS and LES predicted peak frequencies of the pressure in the cavity that were in good agreement with the ones detected in

experiments. Ingress flows were observed but the sealing effectiveness was not quantified.

Cao *et al.*<sup>12</sup> simulated the flow structures in a rotor–stator cavity under axisymmetric annulus flow conditions using URANS. The results showed periodic large-scale structures in the seal gap, which were attributed to the interaction between the annulus and rim seal flows. Boudet *et al.*<sup>13</sup> conducted both steady and unsteady Reynolds-Averaged Navier–Stokes simulations in a rotor–stator system with an axial seal under axis-symmetrical annulus flow conditions. Unsteady results tended to show a decreased sealing effectiveness. The results also showed the three-dimensional and unsteady nature of the ingress flows, which could only be predicted by unsteady solvers. Revert *et al.*<sup>14</sup> experimentally investigated ingress in a rotor–stator system with a chute seal. Sealing effectiveness was once again determined using concentration measurements to study the effect of an axisymmetric axial external flow. The outcome of this study suggested that the complex interaction between the sealing and external flow inevitably leads to ingestion. Burden *et al.*<sup>15</sup> conducted URANS and wall-modelled LES (WMLES) calculations of RI ingress through an axial seal. Both the LES and URANS simulation indicated that the unsteady flow effects dominated the ingress flows in the seal gap. The WMLES results showed less ingestion than URANS at low sealing flow rates, which was attributed to the larger vortical flow structures predicted by URANS.

It should be noted that the topic is also of interest to the wider field of rotating disk flow and the von Kármán swirling flow community.<sup>16</sup> Relevant publications include that of Ravelet *et al.*,<sup>17</sup> who studied the transition to turbulence for an inertially driven von Karman closed flow between two counter-rotating impellers fitted with curved blades.

Although experimental and computational studies have been conducted to investigate RI ingress, there is no direct comparison between predicted and measured RI sealing effectiveness, which quantifies different driving mechanisms of RI ingress (i.e., disk-pumping effect and unsteady flow structures). For the flow structure in wheel-space, the influence of RI ingress on the swirl and pressure distributions is still unclear. Therefore, in this paper, axisymmetric RI ingress experiments are designed and conducted in the simplest form for computational validation. Moreover, unsteady computations are performed to uncover the physics of RI ingress, providing detail beyond the experiments. A computationally inexpensive low-order model is then developed to predict the effect RI ingress has on the wheel-space flow structure.

### III. METHODS

#### A. Experimental methodology

The experimental methodology, the theoretical model, and the computational fluid dynamics (CFD) model are presented in this section, which were used to study the rotationally induced (RI) ingress problem in the absence of an external mainstream gas path flow.

A cross-sectional schematic of the experimental facility is shown in Fig. 3, which comprised of a rotor–stator system; a bladeless rotor and a smooth stator ring platform with no vanes formed a cavity where ingress measurements were collected. The system was open to the atmosphere such that the pressure radially outward of the seal was ambient. The sealing flow was introduced through 16 holes of diameter 6 mm, located radially inboard of the inlet seal. This represented the

purge flow as indicated in Fig. 3 via the blue arrows. The cutaway in Fig. 4 shows the instrumentation located on the stator side of the wheel-space. This included sampling taps on the wall used to measure static pressure and total pressure probes (Pitot) that extended a quarter of the width into the wheel-space; both were also used to sample gas concentration for effectiveness measurements.

The rim seal consisted of an axial clearance formed between the platforms of the stationary and rotating disks at the periphery of the wheel-space. The simple axial seal geometry is shown in Fig. 5. The cavity width between the rotor and the stator in the wheel-space is denoted by  $s$ , whereas the axial rim seal gap is given by  $s_{c,ax}$ . The radial direction is from the inner radius ( $a$ ) to the outer radius ( $b$ ), and the purge flow has a mass flow  $\dot{m}_0$ . Table I presents the test conditions of the rotor–stator system.

**1. Concentration measurements**

The amount of ingress penetrating the rim seal was quantified using a tracer gas technique where the purge flow was seeded with CO<sub>2</sub> at a range of 5000–10 000 ppm (0.5%–1%). The concentration effectiveness in the wheel-space was therefore defined as

$$\varepsilon_c = \frac{c - c_{ref}}{c_0 - c_{ref}}, \tag{1}$$

where  $c$  is the local concentration, with subscripts  $ref$  and 0 denoting ambient conditions and sealing flow rate at the wheel-space inlet, respectively. The ambient concentration had an inherent value of  $c_{ref} \approx 0.045\%$ .

The local concentration,  $c$ , was measured at various locations on the stator disk and in the rotating core, providing circumferential and radial distributions. The radial distribution of concentration was

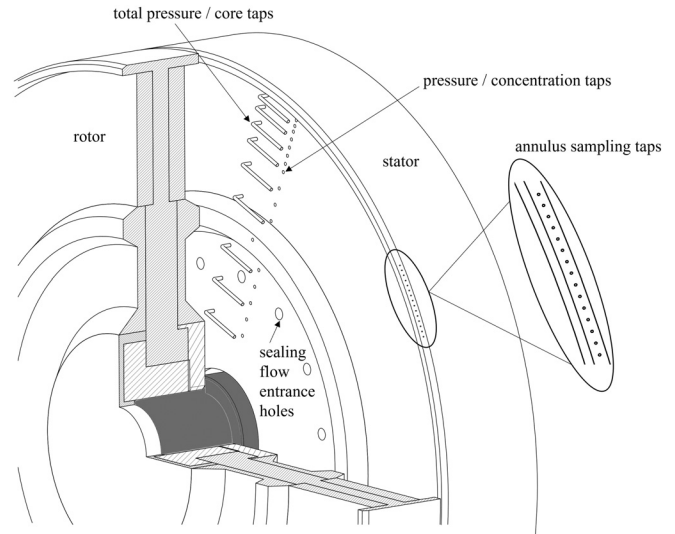


FIG. 4. Rotor–stator cutaway and instrumentation. Sampling taps and immersive probes are used for pressure and concentration measurements.

measured on the stator wall and core using 21 hypodermic taps and 7 immersive bent probes, respectively, as shown in Fig. 4.

The sampling taps were connected to a 20-channel multiplexer, and the concentration was measured using a Signal Group 9000MGA multi-gas analyzer. The multiplexer consists of 20 solenoid valves triggered to sample flow from the location of interest, allowing the effectiveness at a single point in time to be determined. The accuracy, repeatability, and linearity of the analyzer is  $\pm 0.5\%$  of its full-scale

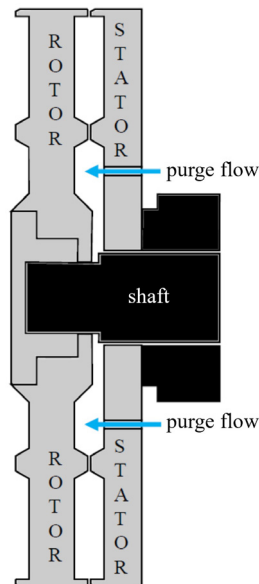


FIG. 3. Schematic of the experimental rig; the rotor–stator system is exposed to ambient conditions at the outer radius, while purge flow can be imposed at the inner radius.

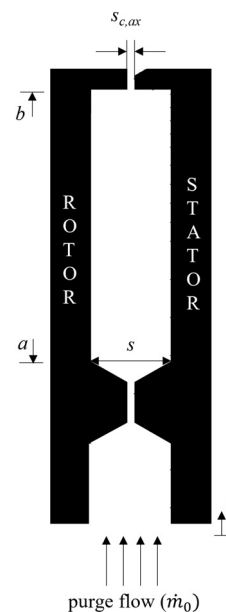


FIG. 5. Schematic of geometric dimensions for the axial seal, showing key parameters and purge flow.

**TABLE I.** Test conditions for different rotational speeds and the range for which each parameter is examined.

| Parameter         | 3000 rpm          | 4000 rpm          |
|-------------------|-------------------|-------------------|
| $Re_\phi$         | $7.4 \times 10^5$ | $9.5 \times 10^5$ |
| $\Phi_0$          | 0–0.1             | 0–0.1             |
| $C_{w,0}$         | 0–4700            | 0–6300            |
| $\dot{m}_0$ (g/s) | 0–6.5             | 0–22              |
| $s_c, ax$ (mm)    | 2                 | 2                 |
| $S$ (mm)          | 20                | 20                |
| $b$ (mm)          | 190               | 190               |
| $a$ (mm)          | 122               | 122               |

range (10 000 ppm). The multiplexer remained at each measurement point until a stable reading was achieved, typically within 30 s, before the concentration was sampled and averaged over 10 s. The ambient levels of CO<sub>2</sub> were monitored regularly, typically before the concentration was measured at a new location. To ensure accurate readings were achieved, the gas analyzer was purged with nitrogen between readings to expel any sample gas that may remain. Calibration of the gas analyzer was completed before the experiments and required the use of high-purity nitrogen gas, which provided the zero-concentration point, and a constant mixture of 8000 ppm (0.8%). Both gases were certified by BOC Ltd.

The sealing flow rate was provided by a pressurized reservoir at 5 bars(g) and was regulated by a Bronkhorst mass flow meter with a controller accuracy (including linearity) of ±0.5% of the reading value plus ±0.1% of the full scale. The sealing flow was mixed with pure CO<sub>2</sub> gas to provide a CO<sub>2</sub> concentration in the range of 0.5%–1%. The sealing flow traveled through a 2 in. diameter pipe, which ensured fully mixed flow occurred before reaching a manifold with the 16 outlets. The sealing flow rate was introduced in the wheel-space through 16 holes at radius  $r/b = 0.45$  below the inner seal, as shown in Fig. 4. As expected, when the sealing flow rate changed, the supplied CO<sub>2</sub> rate changed accordingly such that the air and CO<sub>2</sub> mixture range was maintained. Ambient CO<sub>2</sub> levels were measured far from the experimental rig, but within the same room, to avoid any CO<sub>2</sub> build-up.

The non-dimensional sealing flow rate is defined as

$$C_{w,0} = \frac{\dot{m}_0}{\mu b}, \quad (2)$$

where  $\dot{m}_0$  is the sealing mass flow rate,  $b$  is the radius of the disk periphery, and  $\mu$  is the viscosity. However,  $C_{w,0}$  does not account for the rotational speed of the disk and its geometric characteristics. Therefore, by using the non-dimensional flow parameter  $\Phi_0$ , which is defined as

$$\Phi_0 = \frac{C_{w,0}}{2\pi G_c Re_\phi} = \frac{U}{\Omega b}, \quad (3)$$

the parameters that govern ingress are taken into account. These include the non-dimensional mass flow rate ( $C_{w,0}$ ), geometrical factors such as the ratio between the axial gap distance ( $s_{c,ax}$ ) and disk periphery radius ( $b$ ), denoted by  $G_c$ , and the rotational Reynolds number ( $Re_\phi$ ), which is defined as

$$Re_\phi = \frac{\rho \Omega b^2}{\mu}, \quad (4)$$

where  $\Omega$  is the rotational speed of the rotor. The non-dimensional flow parameter  $\Phi_0$  is implicitly dependent on the viscosity; however, these terms cancel, meaning  $\Phi_0$  is an inviscid parameter.

## 2. Pressure measurements

Pressure measurements in the wheel-space of the experimental facility are taken using a Scanivalve featuring 48 channels, allowing the use of a single differential pressure transducer. This eliminates any systematic error and reduces the overall uncertainty of the results. The pressure settled for 2 s before being sampled and averaged over 2 s at each measurement location.

The radial distribution of static and total pressure was measured using the same taps used for the concentration measurements. The bent probes were immersed in the rotating core at  $z/S = 0.25$ , providing information on the total pressure, the tangential component of velocity ( $v_\phi$ ), and the swirl ratio ( $\beta$ ), defined as

$$\beta(x) = \frac{v_\phi(r)}{\Omega r}, \quad (5)$$

which will be dependent on  $r$ . As the annulus is open to the ambient, the pressure in the wheel-space can reach sub-atmospheric values. An ESI Technology Ltd differential pressure transducer was utilized, ranging between –30 and 30 mbar producing a 0 – 10 V output signal. The combined nonlinearity, hysteresis, and repeatability is given as ≤0.3% of the line of best fit. The transducer was zeroed before the experiments, eliminating the zero and span offset.

## B. Theoretical model

A reduced-order theoretical model is developed here to characterize the flow in the wheel-space. The mathematical representation in Bailey *et al.*<sup>9</sup> is extended to take into consideration the modification of the flow from both ingress and purge flow. The flow structure is assumed to be that in Fig. 2, with boundary layers on both the rotor and the stator separated by a core region. This is justified due to the distance between the two disk surfaces being sufficiently large, such that separate boundary layers are formed on each. The flow in the core region is derived from the Navier–Stokes momentum and continuity equations, assuming steady, inviscid, incompressible, and axisymmetric flow. The theoretical model mandates that the pressure in the core is dependent only on the tangential component of velocity, and any purge flow is entrained into the rotor boundary layer.

For the rotor and stator boundary layers, the flow is assumed to be steady, incompressible, and fully turbulent. It is considered that the fluid axial velocity  $v_z$  is small compared to the other velocity components (radial  $v_r$  and tangential  $v_\phi$ ) and that the pressure depends on the radial direction together with the rate of change of all other variables. It is noted that the boundary layer equations will not be valid near the shroud or the axis of rotation.

Using the above simplifications and assumptions, the governing equations of the fluid flow in a boundary layer are given by

$$\dot{m} = 2\pi r \rho \int_0^\delta v_r dz, \quad (6)$$

$$\frac{d}{dr} \left( r \int_0^\delta v_r^2 dz \right) - \int_0^\delta (v_\phi^2 - v_{\phi,c}^2) dz = -\frac{r}{\rho} \tau_r, \quad (7)$$

$$\frac{d}{dr} \left( r^2 \int_0^\delta v_r (v_\phi - v_{\phi,c}) dz \right) + \frac{\dot{m}}{2\pi\rho} \frac{d}{dr} (rv_{\phi,c}) = -\frac{r^2}{\rho} \tau_\phi, \quad (8)$$

with continuity of mass equation

$$\dot{m}_R + \dot{m}_S = \dot{m}_0. \quad (9)$$

The fluid density is given by  $\rho$  and the shear stress by  $\tau$ . The boundary layer thickness and mass flow rate are given by  $\delta$  and  $\dot{m}$ , respectively. Subscripts  $r$ ,  $\phi$ , and  $c$  denote the radial, circumferential directions, and the core region, respectively, while subscripts  $R$  and  $S$  denote the rotor and stator boundary layers, respectively.

As shown in Bailey *et al.*<sup>9</sup> the velocity profiles in the boundary layers can be approximated using a von Karman 1/7th power law, as they are considered fully turbulent and affected by a moderately favorable pressure gradient. Empirical equations for stresses in smooth pipes are used to determine  $\tau_r$  and  $\tau_\phi$  (see the Appendix for more detail). The system is non-dimensionalized, ensuring key phenomena are captured in the model. These include the rotational Reynolds number,  $Re_\phi$  in Eq. (4), and the swirl ratio,  $\beta$  in Eq. (5). Additionally, the non-dimensional flow rate,  $\lambda$ , with subscript 0 for purge flow and  $I$  for ingress flow, and the non-dimensional radius are defined as

$$\lambda = \frac{\dot{m}}{\mu b} Re_\phi^{-\frac{4}{5}}, \quad x = \frac{r}{b}, \quad (10)$$

where  $x_a \leq x \leq x_b$  and  $x_a$  and  $x_b$  denote the inner and outer non-dimensional radii, respectively.

The non-dimensional expressions above are utilized and the velocity profiles together with the stress terms are substituted in the expressions for the integral momentum equations Eqs. (6)–(8) and continuity equation (9). Detailed derivations of the equations can be found in the Appendix and in Ref. 9. After substantial algebraic manipulation, the set of governing equations for both the rotor and stator boundary layers are derived as

$$\frac{d\alpha_R}{dx} = \frac{\alpha_R}{x(1-\beta)} \left( -\frac{7533}{17150} \frac{(1+\alpha_R^2)^{\frac{3}{8}}}{\alpha_R \gamma_R^{\frac{3}{4}}} + \frac{46(1+8\beta)}{343\alpha_R^2} + 11\beta + 1 + 6x \frac{d\beta}{dx} \right), \quad (11)$$

$$\frac{d\gamma_R}{dx} = \frac{\gamma_R}{x(1-\beta)} \left( \frac{13203}{17150} \frac{(1+\alpha_R^2)^{\frac{3}{8}}}{\alpha_R \gamma_R^{\frac{3}{4}}} - \frac{46(1+8\beta)}{343\alpha_R^2} - \frac{4}{5} (23\beta + 7) - \frac{47x}{5} \frac{d\beta}{dx} \right), \quad (12)$$

$$\frac{d\alpha_S}{dx} = \frac{\alpha_S}{x} \left( \frac{7533}{17150} \frac{(1+\alpha_S^2)^{\frac{3}{8}}}{\alpha_S \gamma_S^{\frac{3}{4}}} - \frac{368}{343\alpha_S^2} - 11 - \frac{6x}{\beta} \frac{d\beta}{dx} \right), \quad (13)$$

$$\frac{d\gamma_S}{dx} = \frac{\gamma_S}{x} \left( -\frac{13203}{17150} \frac{(1+\alpha_S^2)^{\frac{3}{8}}}{\alpha_S \gamma_S^{\frac{3}{4}}} + \frac{368}{343\alpha_S^2} + \frac{92}{5} + \frac{51x}{5\beta} \frac{d\beta}{dx} \right), \quad (14)$$

with

$$\frac{d\beta}{dx} = \frac{144}{49x \left( \alpha_R \gamma_R (1-\beta)^{\frac{3}{5}} + \alpha_S \gamma_S \beta^{\frac{3}{5}} \right)} \left( \frac{5}{6\pi} \lambda_0 x^{-\frac{13}{5}} + \frac{9}{400} \frac{(1+\alpha_R^2)^{\frac{3}{8}} (1-\beta)^{\frac{3}{5}}}{\gamma_R^{\frac{1}{4}}} + \frac{9}{400} \frac{(1+\alpha_S^2)^{\frac{3}{8}} \beta^{\frac{3}{5}}}{\gamma_S^{\frac{1}{4}}} - \frac{49}{60} \alpha_R \gamma_R (1-\beta)^{\frac{3}{5}} \right), \quad (15)$$

and the continuity of mass equation given by

$$\frac{49}{60} \pi x^{\frac{13}{5}} \left( \alpha_R \gamma_R (1-\beta)^{\frac{3}{5}} - \alpha_S \gamma_S \beta^{\frac{3}{5}} \right) = \lambda_0. \quad (16)$$

The ratio of the maximum radial velocity to the relative circumferential velocity between the solid wall and the core is denoted by  $\alpha$ , while  $\gamma$  is the non-dimensional boundary layer thickness with the form

$$\gamma_R = x^{-1} (1-\beta)^{-\frac{3}{5}} (x^2 Re_\phi)^{\frac{1}{5}} \frac{\delta_R}{b}, \quad (17)$$

$$\gamma_S = x^{-1} (x^2 \beta Re_\phi)^{\frac{1}{5}} \frac{\delta_S}{b}. \quad (18)$$

To solve the system of equations [Eqs. (11)–(14)] together with Eq. (16), the sealing flow rate  $\lambda_0$  and initial conditions at the inner radius of the rotor boundary layer ( $\alpha_{R,a}$ ,  $\gamma_{R,a}$ ) and at the outer radius for the stator boundary layer ( $\alpha_{S,b}$ ,  $\gamma_{S,b}$ ) are needed. For the rotor boundary layer at  $x = x_a$ , the measured swirl  $\beta_a$  is utilized as it represents the swirl of the sealing flow at the inlet. The dimensionless boundary thickness  $\gamma_{R,a}$  is then identified from the definition in Eq. (17), assuming a boundary thickness  $\delta_R = S/2$ . The value for  $\alpha_{R,a}$  is found from the continuity of mass equation Eq. (16).

Similarly, for the stator boundary layer at  $x = x_b$ , the swirl  $\beta_b$  is first determined from the conservation of angular momentum in the mixing region beneath the rim seal, as shown in Fig. 6. As it is assumed that the mixing region has a negligible thickness in the radial direction, it follows that

$$\lambda_I \beta_I + \lambda_{R,b} \bar{\beta}_{R,b} = (\lambda_I + \lambda_0) \beta_b + \lambda_{S,b} \bar{\beta}_{S,b}, \quad (19)$$

where the ingress mass flow  $\lambda_I$  is determined from the measured effectiveness [ $\varepsilon = \lambda_0 / (\lambda_0 + \lambda_I)$ ]. As the annulus is open to the atmosphere to create RI conditions, the swirl ratio of the ingress is  $\beta_I = 0$ . The calculations of  $\lambda_{S,b}$ ,  $\lambda_{R,b}$ ,  $\bar{\beta}_{S,b}$ ,  $\bar{\beta}_{R,b}$  are given in the Appendix, Eqs. (A6)–(A9). Consequently,  $\gamma_{S,b}$  is determined from Eq. (18), assuming  $\delta_{S,b} = S/2$ , and  $\alpha_{S,b}$  is calculated using Eq. (16).

As the rotor and stator boundary equations are coupled via the continuity equation, an iterative solver is required to determine the radial distributions of  $\alpha$ ,  $\gamma$ , and  $\beta$ . With the input of the cavity geometry ( $a/b$ ,  $S/b$ ), sealing flow rate ( $\lambda_0$ ), ingress flow rate ( $\lambda_I$ ), ingress swirl ratio ( $\beta_I$ ), measured swirl at  $x = x_a$  ( $\beta_a$ ), and initial guesses of  $\alpha$ ,  $\gamma$ , and  $\beta$ , the solver first updates the initial conditions for both the rotor and stator and solves the boundary layer equations to determine the radial distributions of  $\alpha$  and  $\gamma$ . Due to the stiff nature of the equations, a variable order method in MATLAB is used. After this, the radial distribution of  $\beta$  is updated using the continuity equation. The process is repeated until the maximum change of  $\beta$  is less than a given tolerance ( $10^{-6}$ ). A detailed solution process is given in Fig. 7.

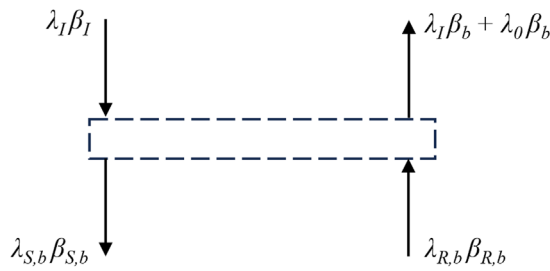


FIG. 6. Control volume for conservation of angular momentum in a mixing region beneath the rim seal.

C. Computational fluid dynamics model

A CFD model was developed in Ansys CFX R19. The model comprises a simplified cavity configuration of a 30° axisymmetric rim-seal sector, including the annulus domain, as shown in Fig. 8. A compressible unsteady RANS approach has been employed with an implicit scheme in time and space. Turbulence closure has been obtained using the fully turbulent  $k-\omega$  SST (Shear Stress Transport) (two-equation) model. The choice of turbulence model was based on the previous experience of Horwood<sup>18</sup> who conducted computations of EI ingress. Unsteady  $k-\omega$  SST simulations were compared with those found using a Reynolds Stress Model (RSM) approach. The increased computational cost of the RSM from the additional transport equations was shown to produce negligible difference in the results. Within the wheel-space, the tangential components of velocity and stress are predominant and flow separation is absent, meaning  $k-\omega$  SST is appropriate. This was confirmed by Mishra *et al.*,<sup>19</sup> where the epistemic uncertainty for RANS modeling was evaluated for a NACA0012 airfoil at different angles of attack. In the absence of laminar separation, the uncertainty was evaluated as negligible. The two-equation  $k-\omega$  SST model is built on the assumption of an isotropic turbulent viscosity and on the Boussinesq hypothesis, which includes the approximation that the Reynolds stress tensor is aligned with the strain tensor of the mean flow. Due to the arrangement of the flow in the problem studied here, the shear is predominantly constant and consequently the shear and Reynolds stresses are aligned, fulfilling the Boussinesq hypothesis.

In the adopted CFD model, the effectiveness has been evaluated by tracing the conservation of CO<sub>2</sub> gas species within air. The balance of the species is dominated by the transport equation for the concentration of CO<sub>2</sub> within the species of air (defined as a constraint). The diffusive term of the transport equation is related to the turbulent viscosity predicted by the model, which is moderated for the RI case and is generally well predicted by RANS.

The imposed boundary conditions include viscous walls with a no-slip condition on the rotor and stator surfaces, two periodic surfaces at the two edges of the domain separated by 30°, swirled purge flow with fixed mass flow rates introduced from the inner seal and pressure far-field or opening away from the cavity. The far-field and opening boundaries in the annulus are set at atmospheric pressure. A gas mixture composed of 99% air and 1% CO<sub>2</sub> was supplied at the lower inlet of the cavity to mimic the experiments. Effectiveness has been evaluated locally using the same definition in Eq. (1) from the experimental procedure.

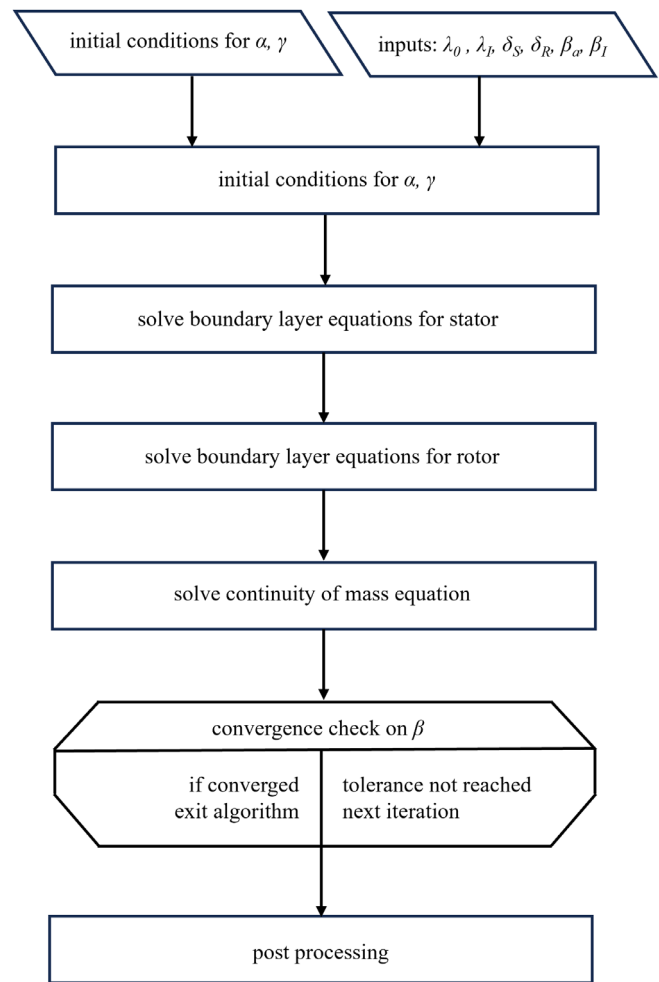


FIG. 7. Solution process used to compute the swirl ratio in the wheel-space.

A non-reactive multi-species approach has been adopted where the diverge terms in the conservation laws are defined including the contribution of each species coupled with the additional constraint that the sum of the concentration of all the species is = 1. Transient simulations have been initialized from a steady RANS solution and the time steps have been set to obtain a physical Courant–Friedrich–Levy (CFL) number of 1.

The 30° sector was generated with an unstructured mesh consisting of  $8 \times 10^6$  elements. The mesh comprises of prismatic elements near the wall for prediction of the boundary layer and tetrahedral elements in the free stream. The height of the first cell close to the wall has been set to obtain an average  $y^+ \approx 2$ , thus the boundary layer has been locally predicted up to the viscous sublayer. Implicit formulation has been employed both in time and space. Convergence has been reached ensuring that residuals drop up to four orders of magnitude for each time step. Unsteady statistics resulted in a steady state for the near wall effectiveness and periodic patterns for selected probes located in the free stream. Convergence is typically obtained after around 8000 core/h on Intel Ivy Bridge nodes mounted on the High-Performance

16 September 2024 07:27:47



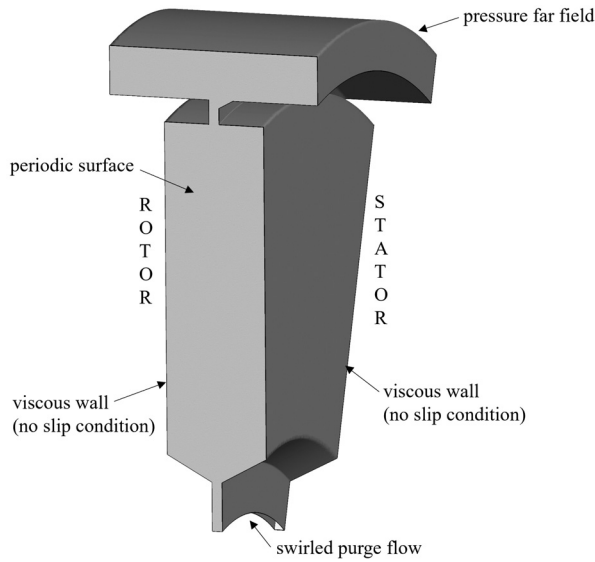


FIG. 8. Computational domain.

Computing (HPC) facility at University of Bath. To speed up the convergence time, computations at different sealing flow rates were initialized from a previously converged unsteady solution.

IV. RESULTS

This section presents combined experimental, theoretical, and computational results that interrogate the phenomena of rotationally induced ingress. The measured sealing effectiveness is first presented, together with the CFD results, which are in excellent agreement. These represent the first computational predictions of effectiveness for RI ingress reported in the literature. The detailed computational flow fields are interrogated to explore the driving mechanisms associated with RI ingress. Second, the pressure and swirl distributions in the wheel-space are considered. The measurements from the experimental facility are compared to the predictions from both the CFD and the 1 D theoretical model of the wheel-space flow.

A. Sealing effectiveness

The measurements of CO<sub>2</sub> concentration are used to quantify ingress in the rotor–stator cavity. Figure 9 shows the radial distribution of effectiveness  $\epsilon_c$  in the wheel-space for three non-dimensional sealing flow rates. Concentration was measured on the stator wall and in the rotating core at 21 and 8 radial positions, respectively, as shown in the silhouette. Data were collected for a constant rotational speed of  $Re_\phi = 9.5 \times 10^5$  for three different purge mass flow rates:  $\Phi_0 = 0.010, 0.018, \text{ and } 0.040$ . The effectiveness measurements show a continuous transition between the three flow regions labeled in Fig. 9.

Region 1—seal clearance: This vicinity is where the ingress and egress momentum exchange occurs; fluid from the ambient with an atmospheric level of CO<sub>2</sub> concentration is entrained into the cavity where it mixes with the sealing flow. The effectiveness is evaluated as defined by Eq. (1), where both the numerator and denominator are scaled by the level of CO<sub>2</sub> naturally present in the atmosphere  $c_{ref}$ . Effectiveness levels increase radially inward from a value of less than

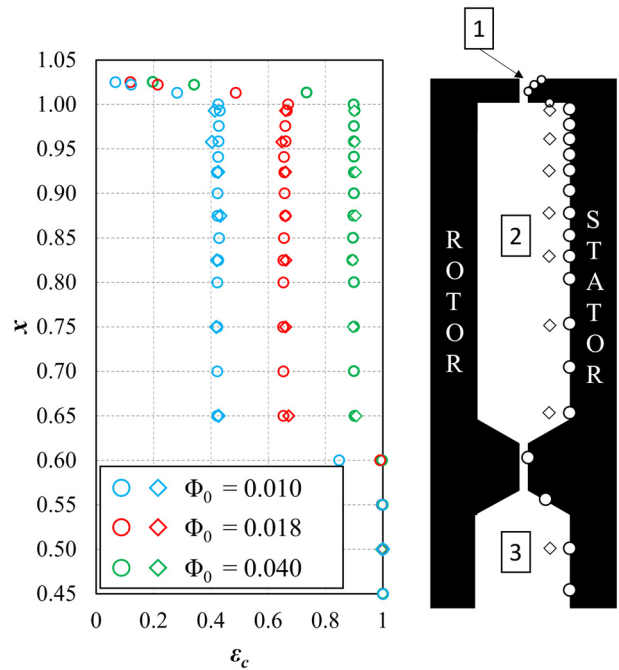


FIG. 9. Radial distribution of effectiveness where circles represent the measured effectiveness on the stator wall and diamonds the measured effectiveness in the core;  $Re_\phi = 7.1 \times 10^5$ .

$\epsilon_c = 0.2$  at the outermost measurement point. The effectiveness in the seal clearance is greater than zero, indicating the presence of egress.

Region 2—main cavity: This is the largest cavity of the experimental configuration, which extends from  $0.65 < x < 1$ . The ingress that penetrates the rim seal gap enters the wheel-space and is further mixed with the sealing flow. In Fig. 9, three profiles are identified, one for each sealing flow rate. The measured effectiveness on the wall and in the fluid core is identical and both are invariant with radius. These two observations lead to the conclusion that the flow can be considered fully mixed in both the axial and radial directions. As expected, increasing the sealing flow rate leads to lower levels of ingress. For  $\Phi_0 = 0.010$ , the effectiveness in Region 2 is equal to 0.41. Introducing additional sealing flow to a value of  $\Phi_0 = 0.018$  increases the effectiveness to  $\epsilon_c = 0.63$ . At the largest sealing flow rate presented of  $\Phi_0 = 0.04$ , the effectiveness is  $\epsilon_c = 0.9$ . At  $x = x_b = 1$ , the effectiveness is measured on the underside of the stator platform, indicated by the circle symbol on the silhouette. This location shows an equivalent value to that measured on the wall and the rotating core at  $x = 0.993$ . This implies that the outer region shown in Fig. 2, where the mixing between ingress and cavity flow occurs, exists across a limited radius for this particular geometry.

Region 3—inner cavity: An inner seal is used radially inward of  $x = x_a = 0.65$ , which creates a second cavity. The inner seal acts as a natural obstacle to the flow path, restricting the radial inflow on the stator side. In this part of the wheel-space, the effectiveness is unity for all three measured purge flow rates, hence no ingress from the above cavity occurs. However, if the purge flow rate is small, it is still possible for ingress to occur (see Fig. 10).

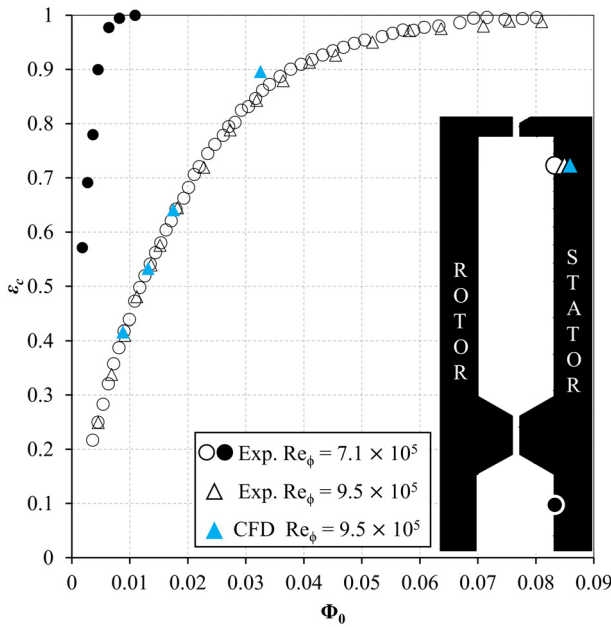


FIG. 10. Effectiveness vs  $\phi_0$  for the inner (solid symbols) and main cavity (open symbols) for two rotational Reynolds numbers  $Re_\phi$  ( $7.1 \times 10^5$  denoted by circles and  $9.5 \times 10^5$  denoted by triangles).

Figure 10 shows the effectiveness at two radial locations in both the main and inner cavities plotted against  $\Phi_0$ . The effectiveness in the main cavity was measured at two  $Re_\phi$  conditions at a radius of  $x = 0.958$ . Data collapse onto a single curve when plotted in this form, demonstrating the inviscid nature of ingress. The effectiveness increases monotonically with  $\Phi_0$  until ingress is prevented at  $\Phi_{min} = 0.068$ . The effectiveness data in the inner cavity (Region 3) show that ingress will penetrate the inner seal but only at minimal sealing flow rates; here, the minimum amount of sealing flow required to prevent ingress in this region is approximately 0.008, almost an order of magnitude less than that of the main cavity.

URANS simulations are conducted for flows at  $Re_\phi = 9.5 \times 10^5$  and four different sealing flow rates,  $\Phi_0 = 0.010, 0.014, 0.018$ , and  $0.033$ . The time-averaged values of the calculated effectiveness at  $x = 0.958$  are presented in Fig. 10, by the solid blue triangles. Note that all  $\Phi_0$  values are sufficiently large, such that ingress does not penetrate the inner cavity. The calculated effectiveness values at  $\Phi_0 \leq 0.018$  are effectively identical to the measured values, while for the higher sealing flow rate  $\Phi_0 = 0.033$  a small over-prediction of effectiveness is observed. The agreement between computational and experimental effectiveness shows that the URANS approach is capable of capturing RI ingress. To the best of the authors' knowledge, this is the first time such agreement has been demonstrated. The result benefits from the design of the RI experiment, which ensures accurate boundary conditions for the CFD model.

The radial distributions of the time-averaged effectiveness from the CFD computations at sealing flow rates of  $\Phi_0 = 0.010$  and  $0.018$  are compared to those measured in the experiments on the stator wall in Fig. 11. The CFD and experimental results are consistent, with little deviation in the effectiveness values between the two in the main cavity

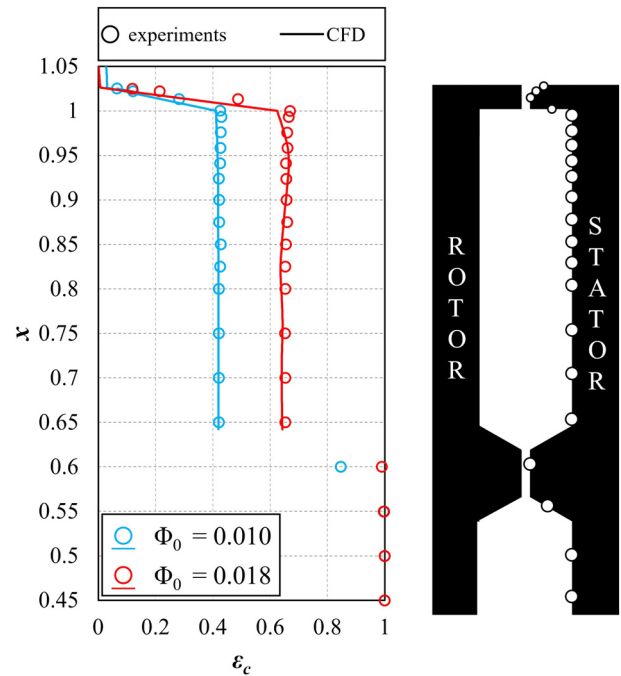


FIG. 11. Radial distribution of effectiveness in the wheel-space. Symbols—experimental data, continuous lines—CFD.

and seal clearance regions. In addition, the CFD results also capture the steep change in effectiveness in the rim seal gap, which again is in good agreement with the experimental data. Figure 12 shows the time-averaged  $x-z$  contours of effectiveness for a sealing flow rate of  $\Phi_0 = 0.018$ . The existence of the region with effectiveness  $\epsilon_c > 0$  radially outboard of the rim seal demonstrates how the egress leaves the wheel-space and is consistent with the effectiveness measurements in the rim seal clearance.

Conventionally, RI ingress is seen as ingress governed by the disk-pumping effect; the low swirl near the stator leads to centripetal ingress in the rim seal clearance, while the high swirl near the rotor results in centrifugal egress. However, recent research has demonstrated the existence of large-scale structures within the seal clearance, including under RI conditions. A key question exists as to what role the structures play in the cause of RI ingress and the mechanism that transports fluid into the cavity.

Figure 13 shows the circumferential variations of effectiveness and radial velocity for instantaneous and time-averaged solutions with a sealing flow rate of  $\Phi_0 = 0.018$ . Snapshots of the effectiveness and radial velocity in the rim seal clearance [Figs. 13(a) and 13(c)] show unsteady structures with alternating regions of ingress and egress. The egress regions indicated by  $v_r > 0$  and ingress regions by  $v_r < 0$  are consistent with the regions of higher and lower concentration effectiveness, respectively. If ingress was caused by the disk-pumping effect within the rim seal gap, regions of ingress would be expected near the stator surface. This can be further explored through the time-averaged results in Figs. 13(b) and 13(d) and the axial variation of the time-averaged radial velocity in Fig. 14. Here, the radial velocities for both the stator and rotor boundary layers are positive. Outside the stator

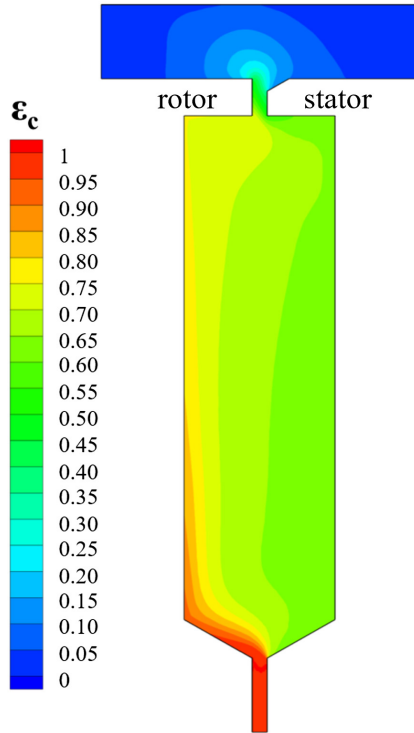


FIG. 12. Effectiveness contours for  $\phi_0 = 0.018$ .

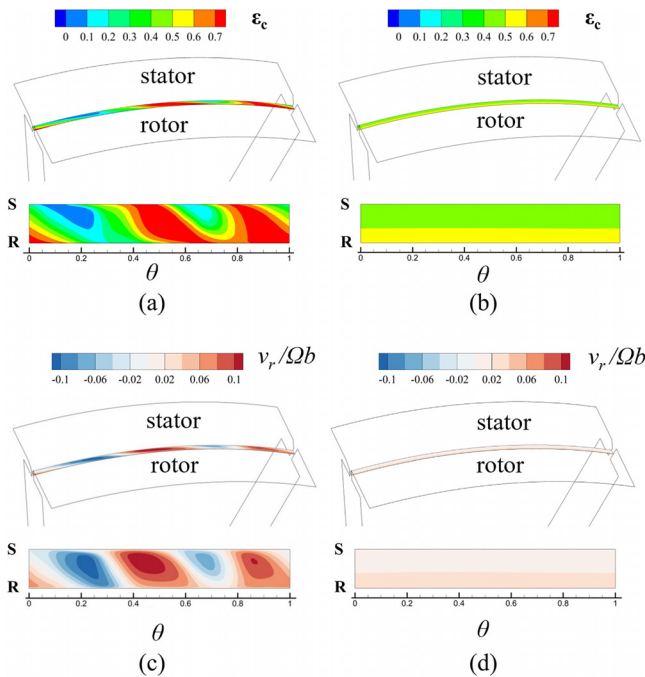


FIG. 13. Circumferential distribution of effectiveness and radial velocity in the rim seal gap. (a) Instantaneous effectiveness, (b) transient average effectiveness, (c) instantaneous radial velocity, and (d) transient average radial velocity.

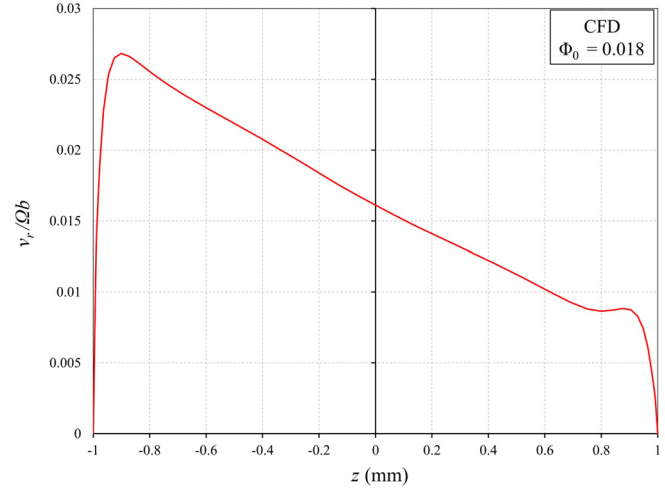


FIG. 14. Normalized time-averaged radial velocity profile across the rim seal gap.

boundary layer, the circumferential variation of radial velocity is larger than that near the rotor boundary layer. This increase can be explained by the strengthened structures near the stator side, leading to a higher radial flux for a fixed pressure difference between the ambient and the wheel-space.

### B. Swirl and pressure measurements and prediction—Flow structure in the wheel-space

While the concentration experiments are representative of ingress, pressure measurements reveal the flow structure in the wheel-space, which is governed by the rotor and stator boundary layers, as discussed in Sec. III B. The rotational motion of the rotor causes the fluid close to it to rotate at a fraction of the disk speed. The fluid velocity in the tangential direction is given by the swirl ratio,  $\beta$ , which controls the radial distribution of the static pressure  $p$  and leads to the definition of the pressure coefficient  $C_p$ ,

$$C_p = \frac{p - p_{ref}}{0.5 \rho \Omega^2 b^2}, \quad (20)$$

where  $p_{ref}$  is a convenient reference pressure, chosen to be at the inner radius of the wheel-space ( $x = x_a = 0.65$ ). Since viscous phenomena are important in the cavity, the turbulent flow parameter  $\lambda_0$  dictates the flow structure, and it can be related to the sealing flow  $\Phi_0$  using

$$\lambda_0 = 2\pi G_c Re_\phi^{0.2} \Phi_0. \quad (21)$$

The results presented for the pressure measurements were conducted at  $Re_\phi = 7.1 \times 10^5$ , resulting in a negligible difference between the magnitudes of the turbulent flow parameter and sealing flow (i.e.,  $\lambda_0 \approx \Phi_0$ ).

The variation of the swirl ratio ( $\beta$ ) and pressure coefficient ( $C_p$ ) against the non-dimensional radius ( $x$ ) is shown in Figs. 15 and 16, respectively. Additionally, CFD results and the corresponding swirl ratio values from the experimental data are included, which are computed using the total and static pressure utilizing Bernoulli's equation to find the tangential component of the velocity  $v_\phi$ , and subsequently the swirl ratio,  $\beta$ . The experimental pressure values were directly

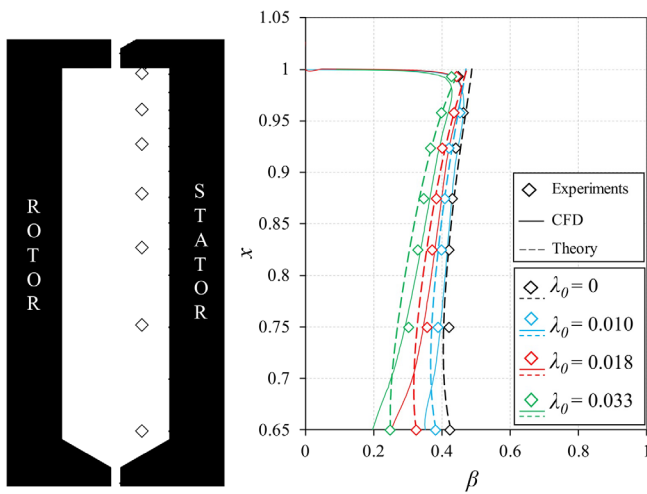


FIG. 15. Radial distribution of swirl ratio,  $\beta$ , in the wheel-space.

measured. The radial locations at which the experimental data were collected for all sealing flow rates are shown in the adjacent silhouettes. For all cases considered, there is a good comparison between the theoretical predictions, CFD results, and the experimental data.

For the zero sealing flow case,  $\lambda_0 = 0$ , the swirl ratio is effectively invariant with radius when  $x < 0.9$  with  $\beta \approx 0.42$ , which is consistent with Daily *et al.*<sup>17</sup> However, for  $0.9 < x < 0.958$  the swirl ratio increases, before decreasing for the outermost measurement location. This decrease is attributed to the low swirl value of the ingress ( $\beta_I = 0$ ). Across all radial locations, the swirl ratio decreases as  $\lambda_0$  increases, which arises due to more angular momentum leaving the cavity. The core rotation speed is reduced as the swirl value increases, however, the swirl ratio has a larger reduction closer to the inner radius, i.e., for  $r/b = 0.65$ .

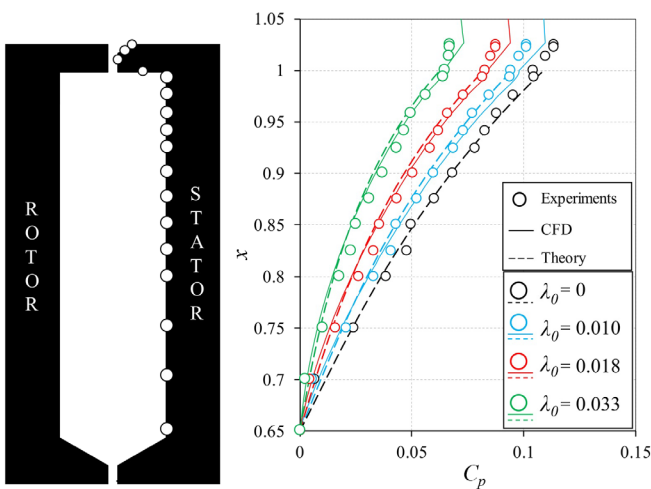


FIG. 16. Radial distribution of pressure coefficient  $C_p$  in the wheel-space and rim seal gap.

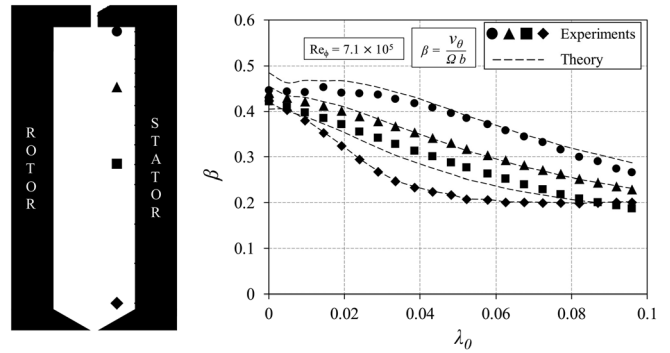


FIG. 17. Variation of swirl ratio with  $\lambda_0$  at four radial positions.

The pressure distributions,  $C_p$ , are consistent with those of the swirl ratio,  $\beta$ , and increase with radius. This is expected due to the positive radial gradient of the static pressure that is caused by the disk-pumping effect of the rotor. Increasing  $\lambda_0$  decreases the pressure coefficient for all radial locations, except at the inner radius as this was selected to be the reference point when calculating  $C_p$ . At  $r/b > 1$ , which is located at the rim seal gap,  $C_p$  remains effectively constant, as these sampling locations are exposed to the ambient air.

Figures 17 and 18 present the corresponding swirl ratio ( $\beta$ ) and pressure distribution ( $C_p$ ) for increasing sealing flow ( $0 \leq \lambda_0 < 0.1$ ) for both the theoretical model and the experimental measurements at given radial locations. Note that the experimental locations are different for the swirl ratio and pressure plots due to the location of the sensors in the experimental facility. The swirl ratio generally decreases as  $\lambda_0$  increases for a fixed radial location. However, for a given  $\lambda_0$  value, the swirl ratio increases as the radial location becomes closer to the outside radius. The pressure distribution follows a similar trend. In both cases, the theoretical predictions match the experimental data well.

The mathematical model shows that the cavity flow structure is affected by the sealing flow rate ( $\lambda_0$ ), the swirl of the sealing flow at the inlet of the cavity ( $\beta_0$ ), the ingress mass flow rate ( $\lambda_I$ ), and the swirl of the ingress mass flow rate ( $\beta_I$ ). Results from Figs. 15–18 give excellent agreement between the theoretical predictions and experimental results, demonstrating that the theory can be used as a practical tool to

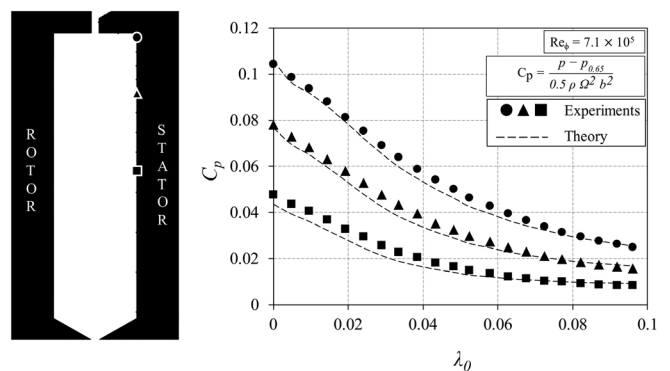


FIG. 18. Variation of pressure coefficient with  $\lambda_0$  at four radial positions.

predict the flow structure in the wheel-space. Thus, the momentum-integral equations can be used to model fluid flow within a rotor–stator system that experiences ingress and superposed sealing flow. Additionally, there was excellent agreement with the CFD predictions. The main advantage of the theoretical model over CFD is the capability to solve the cavity flow field up to four orders of magnitude faster to achieve convergence in terms of computation time, relative to the CFD due to the relative simplicity of the momentum-integral equations. This is beneficial to the iterative engine design process as it allows designers to quickly build up an understanding of how key input parameters can affect the flow structure in the wheel-space and the levels of ingress and egress. Therefore, the reduced-order model provides a computationally cheap solution for preliminary exploration, but more expensive techniques are required for more detailed analysis.

**V. CONCLUSIONS**

This paper presents a combined experimental, computational, and theoretical modeling study of RI ingress in a rotor–stator system. The experimental setup comprised of plain rotor and stator disks, while the boundary radially outboard of the rim seal was open to the atmosphere. Data were collected for two rotational Reynolds numbers with a simple axial clearance seal. The effectiveness and flow structure in the cavity were determined through concentration and pressure measurements, respectively. The experimental results showed that the variation of effectiveness with  $\Phi_0$  collapsed at the two rotational speeds tested. The radial distribution of effectiveness inside the cavity was virtually invariant, indicating that the mixing between the ingress and the sealing flow takes place in a region close to the rim seal. The pressure inside the cavity was sub-atmospheric, with a rotating core present creating a radial pressure gradient that was suppressed with increasing sealing flow. The experimental data serve as a benchmark case that can be used for validating computations of ingress under more complex conditions that include the primary gas path with stator vanes and rotating blades.

To the authors’ knowledge, this is the first time that CFD predictions of effectiveness have been presented for RI ingress. The agreement with the experiments using a turbulence-modelled approach is excellent, capturing close to exact levels of ingress and pressure. Unsteady rotating structures were identified in the rim seal gap that indicated regions of ingress and egress; however, these were not observed in the time-averaged solution, demonstrating that ingress is a time-dependent phenomenon.

It was shown that the momentum-integral equations can be used to model fluid flow within rotor–stator systems with ingress and a superposed sealing flow. There was excellent agreement with the experimental data and CFD predictions, validating the approach. The model shows that the cavity flow structure is affected by the sealing flow rate ( $\lambda_0$ ), the swirl of the sealing flow at the inlet of the cavity, the ingress mass flow rate ( $\lambda_i$ ), and the swirl of the ingress mass flow rate. 1D modeling tools used in industry rely on pressure node networks to estimate sealing mass flow requirements. The theoretical method described here offers the engine designer a computationally inexpensive approach for predicting the flow structure, flow rates, swirl ratios, and pressure in the wheel-space.

**ACKNOWLEDGMENTS**

The authors gratefully acknowledge the University of Bath’s Research Computing Group (doi.org/10.15125/b6cd-s854) for their support in this work.

**AUTHOR DECLARATIONS**

**Conflict of Interest**

The authors have no conflicts to disclose.

**Author Contributions**

**D. Graikos:** Data curation (equal); Formal analysis (equal); Investigation (equal); Validation (equal); Visualization (equal); Writing – original draft (equal). **H. Tang:** Conceptualization (equal); Data curation (equal); Formal analysis (equal); Investigation (equal); Methodology (equal); Supervision (equal); Validation (equal); Writing – original draft (equal); Writing – review & editing (equal). **M. Carnevale:** Data curation (equal); Formal analysis (equal); Methodology (equal); Software (equal); Supervision (equal); Validation (equal); Writing – review & editing (equal). **N. Y. Bailey:** Conceptualization (equal); Formal analysis (equal); Methodology (equal); Supervision (equal); Writing – original draft (equal); Writing – review & editing (equal). **J. A. Scobie:** Conceptualization (equal); Formal analysis (equal); Funding acquisition (equal); Methodology (equal); Project administration (equal); Supervision (equal); Writing – original draft (equal); Writing – review & editing (equal).

**DATA AVAILABILITY**

The data that support the findings of this study are available from the corresponding author upon reasonable request.

**APPENDIX: MATHEMATICAL MODELING OF FLOW IN WHEEL-SPACES**

The velocities on the rotor and stator wall,  $z=0$ , and at the boundary layer thickness,  $z=\delta$ , are

$$\begin{aligned} v_r &= 0, & v_\phi &= V, & \text{at } z &= 0, \\ v_r &= 0, & v_\phi &= v_{\phi,c}, & \text{at } z &= \delta, \end{aligned} \tag{A1}$$

where  $V$  and  $v_{\phi,c}$  are the circumferential velocities on the wall surfaces ( $V_R = \Omega r$ ,  $V_S = 0$ ) and the core ( $v_{\phi,c} = \Omega br$ ), respectively.

Approximated velocity profiles that satisfy the velocity conditions in Eq. (A1) can be used to solve the integral momentum equations (6)–(8). Defining  $\eta = z/\delta$  and using the 1/7th power law profile results in

$$\begin{aligned} v_r(z) &= \alpha(V - v_{\phi,c})\eta^{\frac{1}{7}}(1 - \eta), \\ v_\phi(z) &= V - (V - v_{\phi,c})\eta^{\frac{1}{7}}, \end{aligned} \tag{A2}$$

where

$$\alpha = \frac{v_{r,max}}{(V - v_{\phi,c})}. \tag{A3}$$

Substituting the velocity profiles in Eq. (A2) into the integral momentum equations [Eqs. (6)–(8)] leads to

$$\begin{aligned} \dot{m} &= \frac{49}{60}\pi r \rho \alpha (V - v_c)\delta, \\ \frac{343}{1656} \frac{d}{dr} (r^2 \alpha \delta (V - v_c)^2) & \\ - \delta \left( \frac{1}{8} (V^2 - v_c^2) - \frac{7}{72} (V - v_c)^2 \right) &= -\frac{r}{\rho} \tau_r, \\ \frac{49}{720} \frac{d}{dr} (r^2 \alpha \delta (V - v_c)^2) + \frac{\dot{m}}{2\pi \rho} \frac{d}{dr} (rv_c) &= -\frac{r^2}{\rho} \tau_\phi. \end{aligned} \tag{A4}$$

Expressions for  $\tau_r$  and  $\tau_\phi$  can be formulated using empirical equations for stresses in smooth pipes using the  $1/7^{\text{th}}$  power law profiles, resulting in

$$\begin{aligned}\tau_r &= 0.0225\rho\left(\frac{\mu}{\rho\delta}\right)^{\frac{1}{4}}(V-v_c)^{\frac{7}{4}}\alpha(1+\alpha^2)^{\frac{3}{8}}, \\ \tau_\phi &= -0.0225\rho\left(\frac{\mu}{\rho\delta}\right)^{\frac{1}{4}}(V-v_c)^{\frac{7}{4}}(1+\alpha^2)^{\frac{3}{8}}.\end{aligned}\quad (\text{A5})$$

Using the definitions of  $\lambda$  and  $x$  [in Eq. (10)] together with  $\gamma$  [Eqs. (17) and (18)], the rearranged non-dimensional forms of the momentum equations for the rotor and stator are given by Eqs. (11) and (14).

The non-dimensional flow rate in the rotor and stator boundary layer can be calculated using

$$\lambda_R = \frac{49}{60}\pi\alpha_R\gamma_R x^{\frac{13}{5}}(1-\beta)^{\frac{8}{5}}, \quad (\text{A6})$$

$$\lambda_S = -\frac{49}{60}\pi\alpha_S\gamma_S x^{\frac{13}{5}}\beta^{\frac{4}{5}}. \quad (\text{A7})$$

The averaged swirl in the boundary layer can be determined using

$$\bar{\beta}_R = \frac{\int_0^\delta \rho v_r v_\phi dz}{\Omega r \int_0^\delta \rho v_r dz}, \quad (\text{A8})$$

thus, it follows that

$$\bar{\beta}_R = \frac{5\beta + 1}{6}, \quad \bar{\beta}_S = \frac{5\beta}{6}. \quad (\text{A9})$$

## REFERENCES

- <sup>1</sup>J. A. Scobie, C. M. Sangan, J. M. Owen, and G. D. Lock, "Review of ingress in gas turbines," *J. Eng. Gas Turbines Power* **138**, 120801 (2016).
- <sup>2</sup>J. W. Chew, F. Gao, and D. M. Palermo, "Flow mechanisms in axial turbine rim sealing," *Proc. Inst. Mech. Eng., Part C* **233**, 7637–7657 (2019).
- <sup>3</sup>F. J. Bayley and J. M. Owen, "The fluid dynamics of a shrouded disk system with a radial outflow of coolant," *J. Eng. Power* **92**, 335–341 (1970).
- <sup>4</sup>U. P. Phadke and J. M. Owen, "Aerodynamic aspects of the sealing of gas-turbine rotor-stator systems: Part I: The behavior of simple shrouded rotating-disk systems in a quiescent environment," *Int. J. Heat Fluid Flow* **9**, 98–105 (1988).
- <sup>5</sup>J. W. Chew, S. Dadkhah, and A. B. Turner, "Rim sealing of rotor-stator wheel-spaces in the absence of external flow," *J. Turbomach.* **114**, 433–438 (1992).
- <sup>6</sup>D. J. Graber, W. A. Daniels, and B. V. Johnson, "Disk pumping test," Technical Report No. AWFAL-TR-87-2050 (Pratt and Whitney West Palm Beach FL Government Products Div, 1987).
- <sup>7</sup>C. M. Sangan, O. J. Pountney, K. Zhou, J. M. Owen, M. Wilson, and G. D. Lock, "Experimental measurements of ingestion through turbine rim seals-Part II: Rotationally induced ingress," *J. Turbomach.* **135**, 021013 (2013).
- <sup>8</sup>I. Mear-Stone, "Theoretical modelling of flow in rotor-stator systems," Ph.D. thesis (University of Bath, 2015).
- <sup>9</sup>N. Y. Bailey, J. M. Owen, I. F. Mear, and H. Tang, "Prediction of flows in enclosed rotor-stator cavities," *Phys. Fluids* **34**, 105115 (2022).
- <sup>10</sup>P. F. Beard, F. Gao, K. S. Chana, and J. Chew, "Unsteady flow phenomena in turbine rim seals," *J. Eng. Gas Turbines Power* **139**, 032501 (2017).
- <sup>11</sup>F. Gao, N. Pouljot, J. W. Chew, and P. F. Beard, "Advanced numerical simulation of turbine rim seal flows and consideration for rans turbulence modelling," in *Proceedings of ASME Turbo Expo 2018: Turbomachinery Technical Conference and Exposition* (ASME, 2018), Paper No. GT2018-75116.
- <sup>12</sup>C. Cao, J. W. Chew, P. R. Millington, and S. I. Hogg, "Interaction of rim seal and annulus flows in an axial flow turbine," *J. Eng. Gas Turbines Power* **126**, 786–793 (2004).
- <sup>13</sup>J. Boudet, V. N. D. Autef, J. W. Chew, N. J. Hills, and O. Gentilhomme, "Numerical simulation of rim seal flows in axial turbines," *Aeronaut. J.* **109**, 373–383 (2005).
- <sup>14</sup>A. B. Revert, P. F. Beard, J. W. Chew, and S. Bottenheim, "Sealing performance of a turbine rim chute seal under rotationally-induced ingestion," *J. Phys.: Conf. Ser.* **1909**, 012035 (2021).
- <sup>15</sup>S. Burden, J. W. Chew, F. Gao, and O. Marxen, "Effects of turbine conditions on rim seal performance and prediction," in *Proceedings of the ASME Turbo Expo 2022: Turbomachinery Technical Conference and Exposition* (ASME, 2022), Paper No. GT2022-83194.
- <sup>16</sup>P. Zandbergen and D. Dijkstra, "Von Karman swirling flows," *Annu. Rev. Fluid Mech.* **19**, 465–491 (1987).
- <sup>17</sup>J. W. Daily, W. D. Ernst, and V. V. Asbedian, "Enclosed rotating disks with superposed throughflow: Mean steady and periodic unsteady characteristics of the induced flow," Report No. 64 (Hydrodynamics Laboratory, Department of Civil Engineering, Massachusetts Institute of Technology, 1964).
- <sup>18</sup>J. T. M. Horwood, "Computation of flow instabilities in turbine rim seals," Ph.D. thesis (University of Bath, 2019).
- <sup>19</sup>A. A. Mishra, J. Mukhopadhyaya, G. Iaccarino, and J. Alonso, "Uncertainty estimation module for turbulence model predictions in SU2," *AIAA J.* **57**, 1066–1077 (2019).